Available online at www.sciencedirect.com
ScienceDirect
Trans. Nonferrous Met. Soc. China 29(2019) 1161−1168

Transactions of Nonferrous Metals Society of China
www.tnmsc.cn

Effects of weld penetration on tensile properties of 2219 aluminum alloy TIG-welded joints

Deng-kui ZHANG[1], Yue ZHAO[1,2], Ming-ye DONG[1], Guo-qing WANG[3], Ai-ping WU[1,2,4],
Ji-guo SHAN[1,2], Dan-yang MENG[5], Xian-li LIU[6], Jian-ling SONG[5], Zhong-ping ZHANG[5]

1. Department of Mechanical Engineering, Tsinghua University, Beijing 100084, China;
2. Key Laboratory for Advanced Materials Processing Technology, Ministry of Education, Tsinghua University, Beijing 100084, China;
3. China Academy of Launch Vehicle Technology, Beijing 100076, China;
4. State Key Laboratory of Tribology, Tsinghua University, Beijing 100084, China;
5. Tianjin Long March Launch Vehicle Manufacturing Co., Ltd., Tianjin 300462, China;
6. Capital Aerospace Machinery Corporation Limited, Beijing 100076, China

Received 15 August 2018; accepted 27 February 2019

Abstract: Numerical simulation and experimental methods were used to investigate the effects of weld penetration on tensile properties of 2219 aluminum alloy tungsten inert gas (TIG) welded joints. The results show that when other geometric parameters are consistent, within a certain range, the deeper the weld penetration of the capping weld is, the lower the tensile strength of the joint is. The deeper weld penetration of the capping weld can cause the more concentrated stress at the weld toe and the joint is more likely to crack accordingly. Based on necessary assumptions, a model for analyzing the mathematical relation between the weld penetration of the capping weld and the tensile strength of the joint was proposed to validate the experimental results. The decrease of weld penetration of capping weld can be controlled by decreasing welding current, helium content or increasing welding voltage.

Key words: 2219-C10S aluminum alloy; weld penetration; tensile strength; numerical simulation; correlation

1 Introduction

The tensile properties of fusion-welded joints are very critical in complex welded structures and they can predict whether the welded structures can service safely and successfully. Lacking of fusion or penetration, porosities, slag inclusions and cracks are the most common welding defects that affect the tensile properties of joints [1]. Insufficient weld penetration can result in insufficient combination of two components and the welded joint is prone to fail eventually. However, increasing weld penetration immoderately also easily causes the fracture failure due to overheating of the regions around the weld zone (WZ) [2]. At present, researches on weld penetration mainly focus on how to recognize and control the weld penetration [3−5]. However, there are lack of systematic researches on how the weld penetration affects tensile properties of the welded joint (i.e. the relationship between the weld penetration depth and the tensile properties).

In the manufacturing of large launch vehicles, the tensile properties of some fusion-welded joints are relatively low and unstable, seriously restricting the development of launch vehicles in the aerospace and aviation field. Precipitation-strengthened 2219 aluminum alloy is the main material for cryogenic fuel tanks and inter-stage rings of launch vehicles due to its excellent mechanical properties, weld-ability and stress corrosion resistance. Therefore, researches on the tensile properties of 2219 aluminum alloy welded joints have received extensive attention. There are mainly two methods to improve the tensile properties of 2219 welded joints. One is improving the performance of welds by means of adding refiner to welding wire [6,7], heat-treating after welding [8,9], increasing the agitation of welding

---

Foundation item: Project (U1637601) supported by the Joint Funds of the National Natural Science Foundation of China
Corresponding author: Guo-qing WANG, Tel: +86-10-68756168, E-mail: guoqingwang211@sohu.com;
Ai-ping WU, Tel: +86-10-62773859, E-mail: wuaip@tsinghua.edu.cn
DOI: 10.1016/S1003-6326(19)65024-7

pool [10,11], etc. The other is optimizing the geometry of welds, which involves the regulation of weld reinforcement [12], weld width, mismatch, angular distortion [13], etc. However, there are lack of reports on the regulation of weld penetration in optimizing the geometry of the weld.

In this work, the effects of weld penetration on the tensile properties of 2219 aluminum alloy welded joints were investigated by numerical simulation and experimental methods. This basic work can provide guidance for the further engineering practice.

2 Experimental

The base material was 2219-C10S aluminum alloy plate with the dimensions of 300 mm × 150 mm × 10 mm. C10S involves solution heat-treating and cold working (the deformation is approximately 10%) followed by artificial aging [14,15]. The plates were butt-welded perpendicular to the rolling direction and the filler metal was ER 2325. Table 1 lists the nominal chemical compositions of the 2219 aluminum alloy and the filler metal [16].

Table 1 Chemical compositions of base material and filler metal (mass fraction, %)

Alloy	Si	Fe	Cu	Mn	Mg
2219	0.2	0.3	5.8−6.8	0.2−0.4	0.02
2325	−	−	6.0−6.8	0.2−0.4	−

Alloy	Zn	Ti	Zr	V	Al
2219	0.1	0.02−0.10	0.10−0.25	0.05−0.15	Bal.
2325	−	0.1−0.2	−	−	Bal.

The butt-welded joint was created with a double-layer or a three-layer weld on one side. The combination of direct current tungsten inert gas (DCTIG) arc welding and variable polarity tungsten inert gas (VPTIG) arc welding is one of the widely used welding processes in actual aerospace production. We adopted DCTIG helium-arc welding without a groove and the filler metal as the first layer, and adopted pulse VPTIG argon-arc welding with the filler metal as the second and third layers. Figure 1 shows the schematic illustration of the formation of a three-layer welded joint, and the combination of Figs. 1(a−c) represents the formation process of a double-layer welded joint. Obviously, the weld penetration of the first capping weld depends on the welding process parameters of the first capping weld. It should be noted that the weld penetration of the first capping weld is mainly concerned in this work. For ease of description, “the first capping weld” is replaced by “the capping weld” in the full text.

The specimens used for metallographic observation were cut from the joints perpendicular to the welding direction. After grinding and polishing, the specimens were etched in Keller reagent for 10−15 s. Macroscopic metallographic observation was conducted by optical microscopy (OM), and the specific size measurement was conducted by Photoshop software. The tensile specimens were cut perpendicular to the welding direction according to GB/T 228.1−2010 and the tensile rate was 2 mm/min in the tensile test.

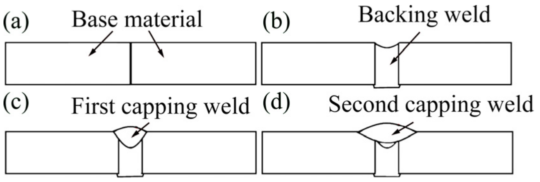

Fig. 1 Schematic illustration of formation of welded joint

The numerical simulation of tensile behaviors of joints was conducted by finite element analysis software (ABAQUS/CAE v6.10-1). According to hardness values and variations of metallographic structure, the profiles of typical regions of joint from the center to both sides were determined, which were WZ, partially melted zone (PMZ), over aged zones (OAZ-1, OAZ-2, OAZ-3, OAZ-4, respectively). Based on our previous work [17], the material parameters of various regions were determined as listed in Table 2.

Table 2 Material parameters of various regions in joint (stress and strain are true stress and true strain, respectively)

Region	Elastic limit stress/MPa	Hardening exponent	Fracturing strain	Maximum stress/MPa
WZ	70	0.31	0.22	312
PMZ	110	0.30	0.14	381
OAZ-1	90	0.31	0.32	375
OAZ-2	155	0.26	0.31	435
OAZ-3	220	0.21	0.31	475
OAZ-4	285	0.16	0.31	523
Base material	349	0.11	0.31	538

3 Results

3.1 Numerical simulation

Six simulation models were calculated. The only geometric variables are the weld penetration of the capping weld, which are 1.5, 2.5, 3.5, 4.5, 6.5 and 8.0 mm for the six models, respectively. The other main geometric parameters of six simulation models are the same and the specific sizes are shown in Table 3. The simulation model diagrams are shown in Fig. 2. The calculated tensile properties are shown in Table 4.

Table 3 Sizes of other main geometric parameters

Front/back weld width/mm	Front/back weld reinforcement height/mm	Distance between weld toe and fusion line of front/back side/mm	Transition angle of weld reinforcement at weld toe of front/back side/(°)
20/8	1.85/1	1/0.6	30/45

Table 4 Calculated tensile properties of simulation models

Weld penetration of capping weld/mm	Tensile strength/MPa	Elongation/%	Cracking strength/MPa	Cracking elongation/%
1.5	317.8	4.91	317.0	3.91
2.5	316.8	4.80	316.8	3.97
3.5	316.6	4.70	316.6	4.10
4.5	312.2	4.65	312.2	3.94
6.5	308.8	4.52	307.7	3.92
8.0	303.8	4.40	301.7	3.73

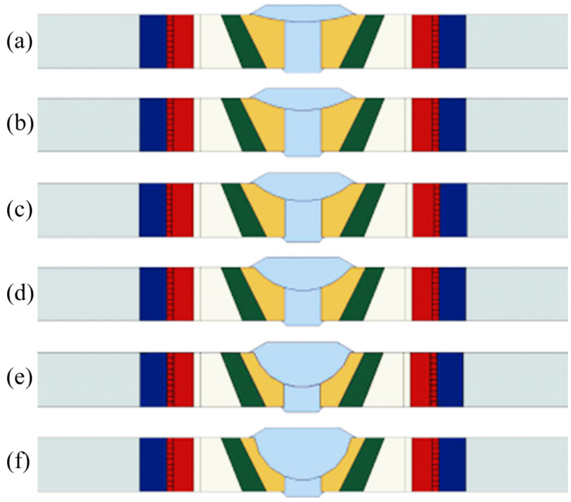

Fig. 2 Simulation model diagrams with capping weld penetrations of 1.5 mm (a), 2.5 mm (b), 3.5 mm (c), 4.5 mm (d), 6.5 mm (e) and 8.0 mm (f)

3.2 Experiments

Twenty-five joints were subjected to the tensile test and each weld penetration of joint of the capping weld was measured. The relationship between the weld penetration of the capping weld and the tensile properties is shown in Fig. 3. In general, within a certain range, the tensile properties decrease as the weld penetration of the capping weld increases. Meanwhile, the correlations between the weld penetration of the capping weld and the tensile properties were analyzed by using the statistical product and service solutions (SPSS) software. The Pearson correlation coefficient between tensile strength and weld penetration of capping weld is −0.810, and between elongation after fracture and weld penetration of capping weld is −0.564. The Pearson correlations is less than zero, and the obvious negative correlation relationships between tensile properties and the weld penetration of the capping weld are verified. It is worth noting that, in actual welding production, it is basically impossible to only change the weld penetration of the capping weld with unchanging other geometric parameters. Therefore, the trends of the relationships in Fig. 3 are not completely linear and the Pearson correlations are not −1. Figure 4 shows the macroscopic metallography of two joints with different weld penetrations of capping weld. For the two joints with penetrations of 6.2 and 5.3 mm, the tensile strengths are 274 and 287 MPa, respectively. The tensile strength exactly increases with the decrease of the weld penetration of the capping weld. Meanwhile, we do see that the geometry of the joint is irregular and there are

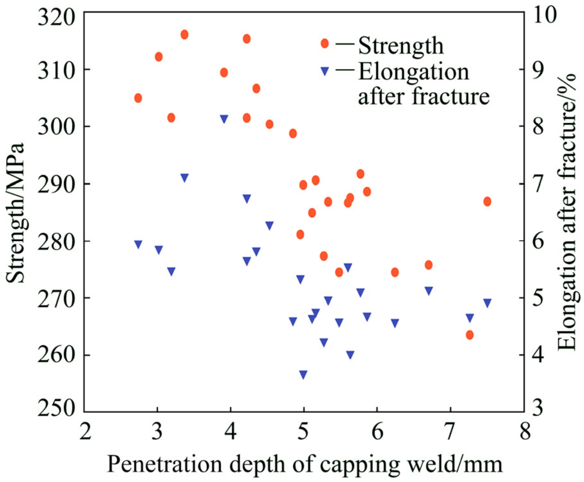

Fig. 3 Tensile properties−penetration depth of capping weld curves of twenty-five welded joints

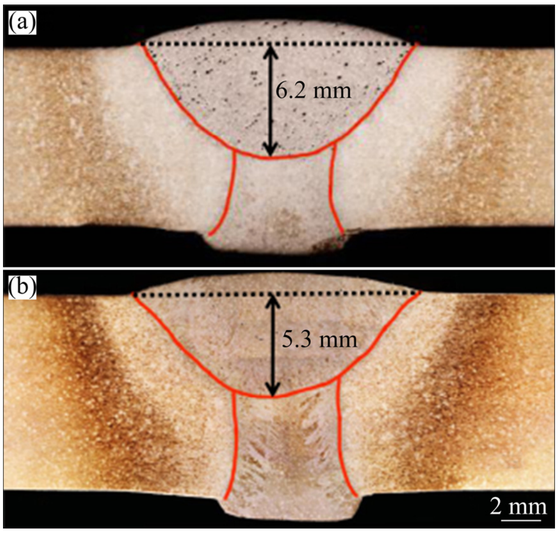

Fig. 4 Macroscopic metallography of joint with weld penetration of capping weld of 6.2 mm (a) and 5.3 mm (b)

many geometric factors that can affect the tensile properties; however, when the other geometric parameters are assumed to be the same, the weld penetration of joint of the capping weld does have a certain correlation relationship with the tensile properties.

4 Reason analysis

4.1 Stress concentration

The numerical results show that the six simulation joints crack at the back weld toe, as shown in Fig. 5. The stress concentration coefficients (K_t represents the first principal stress divided by the nominal stress, K_T represents the equivalent stress divided by the nominal stress) can reflect the stress conditions during the tensile testing. The stress concentration coefficients of the crack initiation point (around the back weld toe) during the tensile testing are extracted, as shown in Fig. 6. Both K_t and K_T increase as the weld penetration of the capping weld increases, indicating that within a certain range, the deeper the weld penetration is, the more concentrated stress has at the back weld toe, and the crack is more likely to occur.

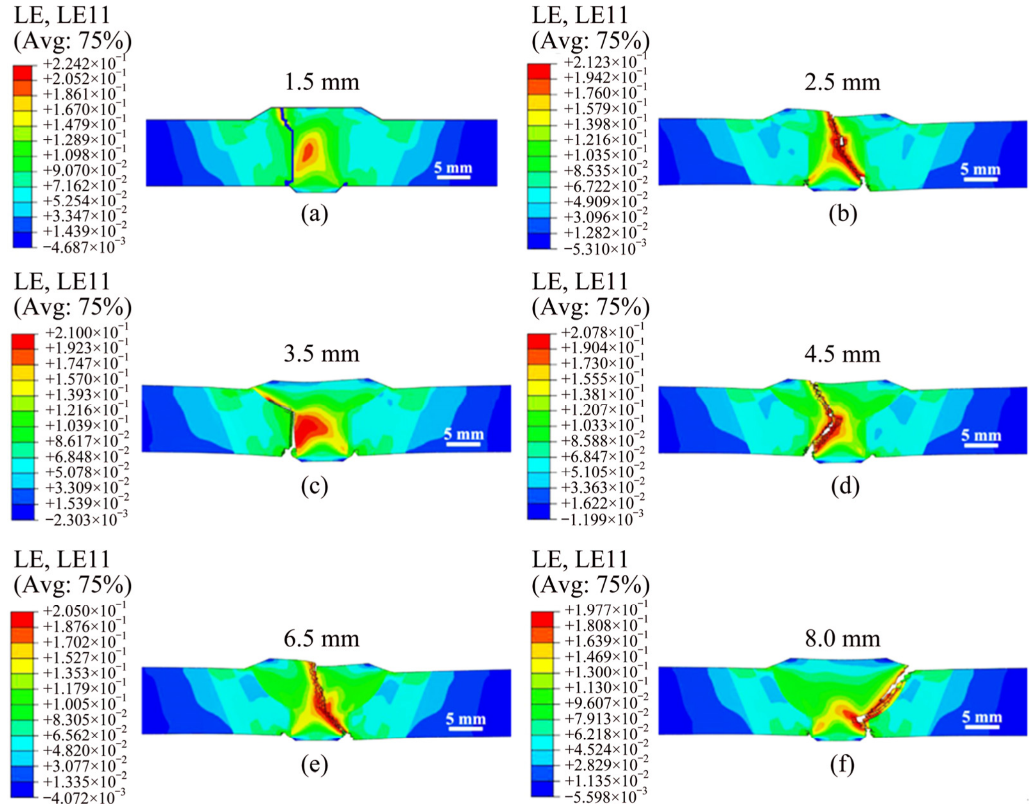

Fig. 5 Strain distributions on edge surface after complete fracture of joint with weld penetration of capping weld of 1.5 mm (a), 2.5 mm (b), 3.5 mm (c), 4.5 mm (d), 6.5 mm (e) and 8.0 mm (f)

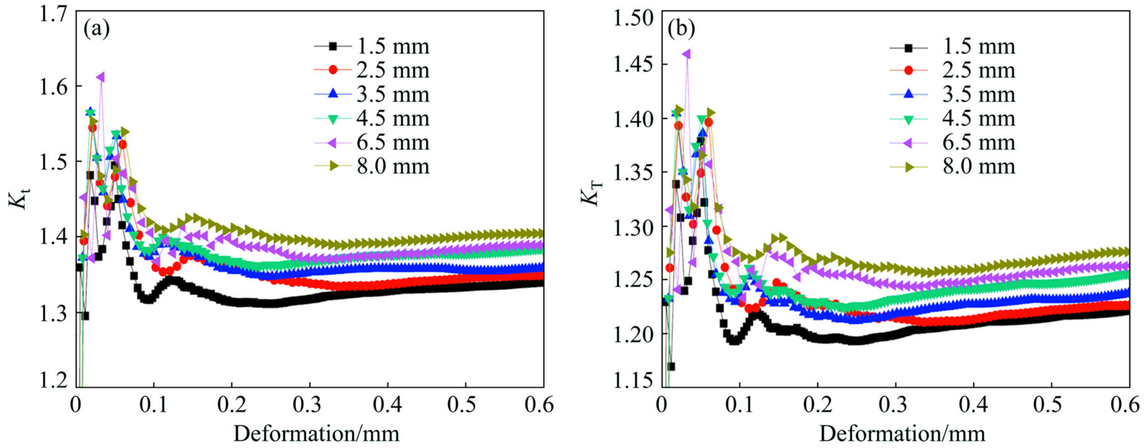

Fig. 6 Stress concentration coefficients during tensile test of joints at different weld penetrations: (a) K_t; (b) K_T

4.2 Modeling and theoretical derivation

The model mainly focuses on the WZ and the effects of weld penetration. In order to simplify the analysis, weld reinforcements are not considered in this model, and the HAZ in this model is a synthesis of five regions of PMZ, OAZ-1, OAZ-2, OAZ-3, and OAZ-4 in numerical simulation.

For the regions of WZ, HAZ and base metal, the strains are $\varepsilon_{\rm w}$, $\varepsilon_{\rm h}$ and $\varepsilon_{\rm b}$, respectively; the strength coefficients are $k_{\rm w}$, $k_{\rm h}$ and $k_{\rm b}$, respectively; the hardening exponents are $n_{\rm w}$, $n_{\rm h}$ and $n_{\rm b}$, respectively; the extension lengths are $\Delta l_{\rm w}$, $\Delta l_{\rm h}$ and $\Delta l_{\rm b}$, respectively. The tensile stress is σ. The transverse total length of the joint is d. The welding plate width is w. The coordinated stress is F_0. The maximum fracture strain of the weld is $\varepsilon_{\max}$.

According to Fig. 7(a), the extension lengths of WZ, HAZ, base metal can be expressed as follows:

$$\Delta l_{\rm w} = a\cdot\varepsilon_{\rm w} = a\cdot\left(\sigma/k_{\rm w}\right)^{1/n_{\rm w}} \tag{1}$$

$$\Delta l_{\rm h} = b\cdot\varepsilon_{\rm h} = b\cdot\left(\sigma/k_{\rm h}\right)^{1/n_{\rm h}} \tag{2}$$

$$\Delta l_{\rm b} = (d-2b-a)\cdot\varepsilon_{\rm b} = (d-2b-a)\cdot\left(\sigma/k_{\rm b}\right)^{1/n_{\rm b}} \tag{3}$$

The workpiece is cut along the ideal interface between the capping weld and the backing weld, and it is divided into the upper and the lower parts with stretching under the average tensile stress.

p_1 and p_2 represent the thickness of the upper part and the lower part of the model, respectively. The extension lengths of the upper and the lower parts can be expressed as follows:

$$\Delta l_1 = a_1\left(\frac{\sigma}{k_{\rm w}}\right)^{\frac{1}{n_{\rm w}}} + 2b_1\left(\frac{\sigma}{k_{\rm h}}\right)^{\frac{1}{n_{\rm h}}} + (d-2b_1-a_1)\left(\frac{\sigma}{k_{\rm b}}\right)^{\frac{1}{n_{\rm b}}} \tag{4}$$

$$\Delta l_2 = a_2\left(\frac{\sigma}{k_{\rm w}}\right)^{\frac{1}{n_{\rm w}}} + 2b_2\left(\frac{\sigma}{k_{\rm h}}\right)^{\frac{1}{n_{\rm h}}} + (d-2b_2-a_2)\left(\frac{\sigma}{k_{\rm b}}\right)^{\frac{1}{n_{\rm b}}} \tag{5}$$

The functional relationship between the extension length and the tensile stress can be expressed as follows:

$$\Delta l_1 = f(\sigma) = a_1\left(\frac{\sigma}{k_{\rm w}}\right)^{\frac{1}{n_{\rm w}}} + 2b_1\left(\frac{\sigma}{k_{\rm h}}\right)^{\frac{1}{n_{\rm h}}} + (d-2b_1-a_1)\left(\frac{\sigma}{k_{\rm b}}\right)^{\frac{1}{n_{\rm b}}} \tag{6}$$

$$\Delta l_2 = F(\sigma) = a_2\left(\frac{\sigma}{k_{\rm w}}\right)^{\frac{1}{n_{\rm w}}} + 2b_2\left(\frac{\sigma}{k_{\rm h}}\right)^{\frac{1}{n_{\rm h}}} + (d-2b_2-a_2)\left(\frac{\sigma}{k_{\rm b}}\right)^{\frac{1}{n_{\rm b}}} \tag{7}$$

The differential forms of the above two equations can be expressed as follows:

$$\mathrm{d}\left[\Delta l_1 = f(\sigma)\right] = \left\{\frac{a_1}{n_{\rm w}}\left(\frac{1}{k_{\rm w}}\right)^{\frac{1}{n_{\rm w}}}\sigma^{\left(\frac{1}{n_{\rm w}}-1\right)} + \frac{2b_1}{n_{\rm h}}\left(\frac{1}{k_{\rm h}}\right)^{\frac{1}{n_{\rm h}}}\sigma^{\left(\frac{1}{n_{\rm h}}-1\right)} + \frac{(d-2b_1-a_1)}{n_{\rm b}}\left(\frac{1}{k_{\rm b}}\right)^{\frac{1}{n_{\rm b}}}\sigma^{\left(\frac{1}{n_{\rm b}}-1\right)}\right\}\mathrm{d}\sigma \tag{8}$$

$$\mathrm{d}\left[\Delta l_2 = F(\sigma)\right] = \left\{\frac{a_2}{n_{\rm w}}\left(\frac{1}{k_{\rm w}}\right)^{\frac{1}{n_{\rm w}}}\sigma^{\left(\frac{1}{n_{\rm w}}-1\right)} + \frac{2b_2}{n_{\rm h}}\left(\frac{1}{k_{\rm h}}\right)^{\frac{1}{n_{\rm h}}}\sigma^{\left(\frac{1}{n_{\rm h}}-1\right)} + \frac{(d-2b_2-a_2)}{n_{\rm b}}\left(\frac{1}{k_{\rm b}}\right)^{\frac{1}{n_{\rm b}}}\sigma^{\left(\frac{1}{n_{\rm b}}-1\right)}\right\}\mathrm{d}\sigma \tag{9}$$

The variations of the total extension lengths of the upper and the lower parts caused by the tiny coordinated stress $\mathrm{d}F_0$ are s_1, s_2, respectively, and they have the following relationship equations:

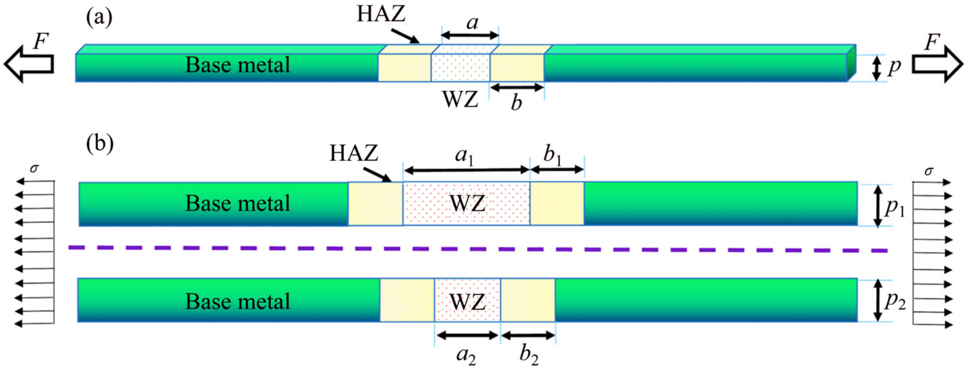

Fig. 7 Analytical model: (a) Regional division and overall force; (b) Model decomposition, including upper and lower parts

$$\frac{s_1}{s_2}=\frac{f'(\sigma)\mathrm{d}\sigma}{F'(\sigma)\mathrm{d}\sigma}=\frac{f'(\sigma)\dfrac{\mathrm{d}F_0}{w\cdot p_1}}{F'(\sigma)\dfrac{\mathrm{d}F_0}{w\cdot p_2}} \tag{10}$$

$$s_1=\frac{f'(\sigma)p_2}{F'(\sigma)p_1}s_2 \tag{11}$$

According to Fig. 8, the coordination relationship of extension lengths can be expressed as follows:

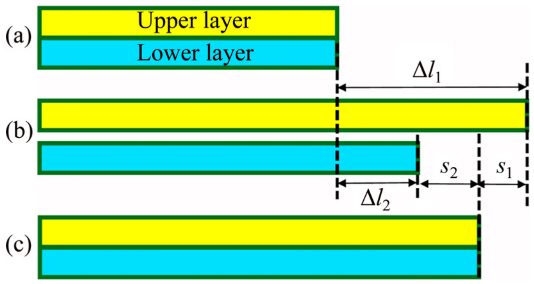

Fig. 8 Changes of total extension lengths of upper and lower parts caused by tiny coordinated stress: (a) Before tensile testing; (b) Assumption; (c) After tensile testing

$$\Delta l_1-\Delta l_2=s_1+s_2 \tag{12}$$

Combined with Eqs. (11) and (12), we can get

$$s_1=(\Delta l_1-\Delta l_2)\frac{f'(\sigma)p_2}{f'(\sigma)p_2+F'(\sigma)p_1} \tag{13}$$

$$s_2=(\Delta l_1-\Delta l_2)\frac{F'(\sigma)p_1}{f'(\sigma)p_2+F'(\sigma)p_1} \tag{14}$$

The total extension length during the tensile can be expressed as follows:

$$\Delta l_{\text{total}}=s_2+\Delta l_2=\Delta l_1\frac{F'(\sigma)p_1}{f'(\sigma)p_2+F'(\sigma)p_1}+\Delta l_2\frac{f'(\sigma)p_2}{f'(\sigma)p_2+F'(\sigma)p_1} \tag{15}$$

In the total extension length, the extension lengths of the upper and the lower parts can be expressed as

$$\Delta l_{\text{w}(\text{total}_1)}=\Delta l_{\text{total}}\{a_1\left(\frac{\sigma}{k_\text{w}}\right)^{\frac{1}{n_\text{w}}}/[a_1\left(\frac{\sigma}{k_\text{w}}\right)^{\frac{1}{n_\text{w}}}+2b_1\left(\frac{\sigma}{k_\text{h}}\right)^{\frac{1}{n_\text{h}}}+(d-2b_1-a_1)\left(\frac{\sigma}{k_\text{b}}\right)^{\frac{1}{n_\text{b}}}]\} \tag{16}$$

$$\Delta l_{\text{w}(\text{total}_2)}=\Delta l_{\text{total}}\{a_2\left(\frac{\sigma}{k_\text{w}}\right)^{\frac{1}{n_\text{w}}}/[a_2\left(\frac{\sigma}{k_\text{w}}\right)^{\frac{1}{n_\text{w}}}+2b_2\left(\frac{\sigma}{k_\text{h}}\right)^{\frac{1}{n_\text{h}}}+(d-2b_2-a_2)\left(\frac{\sigma}{k_\text{b}}\right)^{\frac{1}{n_\text{b}}}]\} \tag{17}$$

Considering that the WZ is the weakest region, the WZ can fracture failure when the tensile strain of the WZ reaches the maximum fracture strain of the material. Taking the lower part of WZ as an example, it has the following equation when failing (the tensile stress is the ultimate tensile strength in this equation):

$$\varepsilon_\text{w}=\varepsilon_{\max}=\Delta l_{\text{total}}\{\left(\frac{\sigma_\text{m}}{k_\text{w}}\right)^{\frac{1}{n_\text{w}}}/[a_2\left(\frac{\sigma_\text{m}}{k_\text{w}}\right)^{\frac{1}{n_\text{w}}}+2b_2\left(\frac{\sigma_\text{m}}{k_\text{h}}\right)^{\frac{1}{n_\text{h}}}+(d-2b_2-a_2)\left(\frac{\sigma_\text{m}}{k_\text{b}}\right)^{\frac{1}{n_\text{b}}}]\} \tag{18}$$

Combining Eqs. (4), (5), (8), (9), (15) and (18), the relationship between the maximum fracture strain and the ultimate tensile strength can be obtained as follows:

$$\begin{aligned}\varepsilon_{\max}=&\{\sum_{i=1}^{2}\Delta l_i p_i(\frac{a_{i+(-1)^{i+1}}}{n_\text{w}}\left(\frac{1}{k_\text{w}}\right)^{\frac{1}{n_\text{w}}}\sigma^{\left(\frac{1}{n_\text{w}}-1\right)}+\\&\frac{2b_{i+(-1)^{i+1}}}{n_\text{h}}\left(\frac{1}{k_\text{h}}\right)^{\frac{1}{n_\text{h}}}\sigma^{\left(\frac{1}{n_\text{h}}-1\right)}+\\&\frac{\left(d-2b_{i+(-1)^{i+1}}-a_{i+(-1)^{i+1}}\right)}{n_\text{b}}\cdot\\&\left(\frac{1}{k_\text{b}}\right)^{\frac{1}{n_\text{b}}}\sigma^{\left(\frac{1}{n_\text{b}}-1\right)})\}\cdot\{\sum_{i=1}^{2}p_{i+(-1)^{i+1}}(\frac{a_i}{n_\text{w}}\left(\frac{1}{k_\text{w}}\right)^{\frac{1}{n_\text{w}}}\cdot\\&\sigma^{\left(\frac{1}{n_\text{w}}-1\right)}+\frac{2b_i}{n_\text{h}}\left(\frac{1}{k_\text{h}}\right)^{\frac{1}{n_\text{h}}}\sigma^{\left(\frac{1}{n_\text{h}}-1\right)}+\\&\frac{(d-2b_i-a_i)}{n_\text{b}}\left(\frac{1}{k_\text{b}}\right)^{\frac{1}{n_\text{b}}}\sigma^{\left(\frac{1}{n_\text{b}}-1\right)})\}^{-1}\cdot\\&\left(\frac{\sigma_\text{m}}{k_\text{w}}\right)^{\frac{1}{n_\text{w}}}(a_2\left(\frac{\sigma_\text{m}}{k_\text{w}}\right)^{\frac{1}{n_\text{w}}}+2b_2\left(\frac{\sigma_\text{m}}{k_\text{h}}\right)^{\frac{1}{n_\text{h}}}+\\&(d-2b_2-a_2)\left(\frac{\sigma_\text{m}}{k_\text{b}}\right)^{\frac{1}{n_\text{b}}})^{-1}\end{aligned} \tag{19}$$

If only the extension length of the WZ is considered, the HAZ and the base metal are regarded as the rigid bodies. The following formula can be obtained:

$$\varepsilon_{\max}=\frac{a_2(p_1+p_2)(\sigma_\text{m}/k_\text{w})^{1/n_\text{w}}}{a_2p_1+a_1p_2} \tag{20}$$

The k_w, n_w and $\varepsilon_{\max}$ values are 491.3, 0.31 and 0.22, respectively [17]. We can get

$$\sigma_\text{m}=311.9418\times\left((p_1+\frac{a_1}{a_2}p_2)/p\right)^{\frac{3}{10}} \tag{21}$$

When a_1 and a_2 are certain (i.e. both the front weld width and the back weld width are certain), the larger the p_2 is (i.e. the smaller the weld penetration of the capping weld is), the larger the σ_m is. That is, within a certain range, the deeper the weld penetration of the capping weld is, the lower the tensile strength is. The results obtained from the above model analysis are agreement with those obtained from experiments.

5 Control methods

For the welded joints, weld penetration of the capping weld mainly depends on the welding process parameters of the capping weld, including welding current, welding voltage, welding speed, wire feeding speed, shielding gas flow rate and helium content, etc. In the prior experiments, welding speed of the capping weld was almost the same. Meanwhile, according to the analysis of the SPSS, the weld penetration of the capping weld is independent of the wire feeding speed. Therefore, the relationships between the weld penetration of the capping weld (y) and welding current (x_1), welding voltage (x_2), helium content (x_3) of the capping weld were analyzed using the SPSS, and the analysis results are shown in Table 5, the linear relation can be approximately expressed as: $y=0.001x_1-0.084x_2+0.924x_3+4.961$. This indicates that the weld penetration of the capping weld increases with the increase of welding current, helium content, or decreases with the increase of welding voltage. In actual production, the weld penetration of the capping weld can be controlled by adjusting welding current, welding voltage and helium content of the capping weld.

Table 5 Linear regression analysis between weld penetration and welding process parameters of capping weld

Process parameters of capping weld	Unstandardized coefficients		Standardized coefficient β	t	Significance
	B	Std. error			
Constant	4.961	5.426	−	0.914	0.371
Welding current/A	0.001	0.015	0.017	0.082	0.935
Welding voltage/V	−0.084	0.288	−0.064	−0.292	0.773
Helium content/ ($\mathrm{L\cdot min^{-1}}$)	0.924	0.327	0.558	2.829	0.010

6 Conclusions

(1) The results of these experiments and simulations indicate that within a certain range, when other geometric parameters are consistent, the tensile properties decrease with the increase of the weld penetration of the capping weld.

(2) A model is proposed for analyzing the relationship between the weld penetration of the capping weld and tensile strength of the joint, and the conclusion is in good agreement with the experimental and numerical simulation results.

(3) The weld penetration of the capping weld increases with the increase of welding current, helium content or decreases with the increase of welding voltage. These welding process parameters should be considered comprehensively to get a proper weld penetration.

References

[1] DESHMUKH A R, VENKATACHALAM G, DIVEKAR H, SARAF M R. Effect of weld penetration on fatigue life [J]. Procedia Engineering, 2014, 97: 783−789.

[2] WU Yong-chao, ZHONG Qiu, CHEN Zhen-yu, ZHANG Chu-zhong. The best penetration of fusion welding for sheet metal [J]. Physical testing and chemical analysis (part a): Physical testing, 2014, 50(5): 347−350.

[3] TRAIDIA A, ROGER F. A computational investigation of different helium supplying methods for the improvement of GTA welding [J]. Journal of Materials Processing Technology, 2011, 211(9): 1553−1562.

[4] CHEN Chen, WEI Xin-qian, ZHAO Yong, YAN Keng, JIA Zhan-jun, HE Yu-xiang. Effects of helium gas flow rate on arc shape, molten pool behavior and penetration in aluminum alloy DCEN TIG welding [J]. Journal of Materials Processing Technology, 2018, 255: 696−702.

[5] KOU S, SUN D K. Fluid flow and weld penetration in stationary arc welds [J]. Metallurgical and Materials Transactions A, 1985, 16: 203−213.

[6] KISHORE B N, PAN D, SUN Z, WEI J, TALARI M K. Effect of titanium-boron additions on grain refinement of AA 2219 gas tungsten arc welds [J]. Science and Technology of Welding and Joining, 2012, 17(5): 386−393.

[7] NAGA R P, SRINIVASA R K, REDDY G M, KAMARAJ M, PRASAD R K. Microstructure and high temperature stability of age hardenable AA2219 aluminium alloy modified by Sc, Mg and Zr additions [J]. Materials Science and Engineering A, 2007, 464(1−2): 192−201

[8] LIN Yi-tong, WANG Ming-chao, ZHANG Yu, HE Ya-zhang, WANG Dong-po. Investigation of microstructure evolution after post-weld heat treatment and cryogenic fracture toughness of the weld metal of AA2219 VPTIG joints [J]. Materials and Design, 2017, 113: 54−59.

[9] MALARVIZHI S, BALASUBRAMANIAN V. Influences of welding processes and post-weld ageing treatment on mechanical and metallurgical properties of AA2219 aluminium alloy joints [J]. Welding in the World, 2012, 56: 105−119.

[10] QIU L, YANG C L, LIN S B, FAN C L. Effect of pulse current on microstructure and mechanical properties of variable polarity arc weld bead of 2219-T6 aluminium alloy [J]. Materials Science and Technology, 2009, 25(6): 739−742.

[11] KOTESWARA R S, MADHUSUDHANA R G, KAMARAJ M, PRASAD R K. Grain refinement through arc manipulation techniques in Al−Cu alloy GTA welds [J]. Materials Science and Engineering A, 2005, 404(1−2): 227−234.

[12] WANG Guo-qing, LI Quan, LI Yan-jun, WU Ai-ping, MA Ning-xu, YAN Dong-yang, WU Hui-qiang. Effects of weld reinforcement on tensile behavior and mechanical properties of 2219-T87 aluminum

alloy TIG welded joints [J]. Transactions of Nonferrous Metals Society of China, 2017, 27(1): 10−16.

[13] GORDON S S. An investigation into geometry and microstructural effects upon the ultimate tensile strengths of butt welds [R]. Washington DC: NASA Marshall Space Flight Center, 1992.

[14] ZHANG Deng-kui, LI Quan, ZHAO Yue, LIU Xian-li, SONG Jian-ling, WANG Guo-qing, WU Ai-ping. Microstructure and mechanical properties of three-layer TIG-welded 2219 aluminum alloys with dissimilar heat treatments [J]. Journal of Materials Engineering and Performance, 2018, 27(6): 2938−2948.

[15] ZHANG Deng-kui, WANG Guo-qing, WU Ai-ping, ZHAO Yue, LI Quan, LIU Xian-li, MENG Dan-yang, SONG Jian-ling, ZHANG Zhong-ping. Study on the inconsistency in mechanical properties of 2219 aluminium alloy TIG-welded joints [J]. Journal of Alloys and Compounds, 2019, 777: 1044−1053.

[16] LI Quan, WU Ai-ping, ZHAO Yue, WANG Guo-qing, YAN Dong-yang, WU Hui-qiang. Fracture behavior of double-pass TIG welded 2219-T8 aluminum alloy joints under transverse tensile test [J]. Transactions of Nonferrous Metals Society of China, 2015, 25(6): 1794−1803.

[17] LI Yan-jun, LI Quan, WU Ai-ping, MA Ning-xu, WANG Guo-qing, MURAKAWA H, YAN Dong-yang, WU Hui-qiang. Determination of local constitutive behavior and simulation on tensile test of 2219-T87 aluminum alloy GTAW joints [J]. Transactions of Nonferrous Metals Society of China, 2015, 25(9): 3072−3079.

焊缝熔深对 2219 铝合金 TIG 焊接头拉伸性能的影响

张登魁[1]，赵 玥[1,2]，董明晔[1]，王国庆[3]，吴爱萍[1,2,4]，
单际国[1,2]，蒙丹阳[5]，刘宪力[6]，宋建岭[5]，张中平[5]

1. 清华大学 机械工程系，北京 100084；
2. 清华大学 先进成形制造教育部重点实验室，北京 100084；
3. 中国运载火箭技术研究院，北京 100076；
4. 清华大学 摩擦学国家重点实验室，北京 100084；
5. 天津航天长征火箭制造有限公司，天津 300462；
6. 首都航天机械公司，北京 100076

摘 要：采用数值模拟和实验的方法研究焊缝熔深对 2219 铝合金 TIG 焊接头拉伸性能的影响。结果表明，当其他几何参数一致时，在一定范围内，盖面焊缝的熔深越大，接头的拉伸性能越低。较大的盖面焊缝熔深可造成焊趾处更集中的应力，导致接头更容易断裂。根据必要的假设提出的一种分析盖面熔深与接头拉伸性能间数学关系的模型验证了实验结论。盖面焊缝熔深的减少可通过降低焊接电流、氦气流量或增加焊接电压来调控。

关键词：2219-C10S 铝合金；焊缝熔深；拉伸强度；数值模拟；相关性

(Edited by Xiang-qun LI)